

Seeing Molecules by Eye: Surface Plasmon Resonance Imaging at Visible Wavelengths with High Spatial Resolution and Submonolayer Sensitivity**

Jimin Yao, Matthew E. Stewart, Joana Maria, Tae-Woo Lee, Stephen K. Gray, John A. Rogers,* and Ralph G. Nuzzo*

Surface plasmon resonance (SPR) spectroscopy provides a powerful method for fully label free forms of biological and chemical detection.^[1–3] These measurements exploit the extreme sensitivity of plasmons to changes in refractive index occurring at a metal/dielectric interface^[1,4–7] and can be carried out (most commonly) singularly or in a multiplexed fashion by using imaging-mode protocols.^[6,8,9] Most SPR sensors employ the Kretschmann configuration, which uses a prism to couple light into plasmons at the metal surface. This geometry is difficult to integrate into low-cost, portable devices for high-throughput applications.^[10–12] We and others have shown that these limitations can be circumvented by using grating couplers in the form of periodic nanohole arrays,^[10,13–16] a device form factor that can enable powerful new forms of multispectral, spectroscopic, and multiplexed imaging-mode assays.

For example, we recently demonstrated one-dimensional plasmonic imaging with micrometer spatial resolution and

monolayer sensitivity using quasi-three-dimensional (quasi-3D) plasmonic crystals as sensing optic.^[13] The precise structural definition of these crystals, formed by depositing gold by electron beam evaporation onto a periodic nanowell array embossed in a thin polymer film, provides a uniformity sufficient to both quantitatively model their optical response by full 3D finite-difference time-domain (FDTD) calculations and to effect quantitative 1D and 2D imaging-mode measurements of protein binding interactions.^[12] The one caveat was that the design rule of the plasmonic crystal optic (nanowell diameter, depth, and center-to-center spacing of about 480, 350, and 780 nm, respectively) and its quasi-3D form factor (a gold nanohole array with a separate layer of gold disks at the bottom of the embossed nanowells) provided an optical sensitivity that fell largely in the near-infrared region. Simple, low-cost assays require optics that, while retaining the rugged characteristics of these plasmonic crystals, provide significant sensitivity at visible wavelengths. It is generally presumed that shifting the energy spectrum of the plasmonic crystal optic in this way would require significantly altering the design rules of the device, that is, using much finer dimensions for the embossed grating and thereby greatly increasing demand tolerances for its spatial uniformity as well as the cost and complexity of the required lithographic mastering protocols.

We describe here a new type of easily fabricated plasmonic crystal optic—a fully integrated 3D plasmonic crystal—that provides exceptional analytical sensitivity at visible wavelengths, sufficient to detect with high spatial resolution molecular binding events that can differentiate adsorbates whose masses differ by as little as 25 amu. As confirmed by FDTD calculations, the enhanced sensitivity obtained in the visible region of the spectrum comes not solely from confinement effects but also from the consequences of the complex interactions of the various diffractive and plasmonic modes supported by this device form factor. Most significantly, the new plasmonic crystal optic allows molecular imaging with high sensitivity by using a common optical microscope and low-cost silicon charge-coupled device (CCD) camera, which has significant implications for the development of cheap, highly sensitive, and compact form-factor devices useful for the detection of biological and chemical agents.

Square arrays of cylindrical nanowells were molded into the surface of UV-curable polyurethane by a soft nanoimprint technique^[11] that yields large-area, spatially uniform arrays suitable for SPR imaging applications (Supporting Information, Figure S1). The diameter, depth, and periodicity of the

[*] J. Maria, Prof. J. A. Rogers

Department of Materials Science and Engineering, Frederick Seitz Materials Research Laboratory, University of Illinois
104 S. Goodwin Ave., MC-230 Urbana, IL 61801 (USA)
Fax: 217-333-2736
E-mail: jrogers@uiuc.edu

J. Yao, M. E. Stewart, Prof. R. G. Nuzzo
Department of Chemistry, University of Illinois
South Mathews Avenue, Urbana, IL 61801 (USA)
Fax: 217-244-2278
E-mail: r-nuzzo@uiuc.edu

Dr. T.-W. Lee
Center for Computation & Technology, 216 Johnston Hall
Louisiana State University, Baton Rouge, LA 70803 (USA)

Dr. S. K. Gray
Chemistry Division and Center for Nanoscale Materials
Argonne National Laboratory, Argonne, Illinois 60439 (USA)

[**] This work was carried out in part in the Frederick Seitz Materials Research Laboratory Central Facilities, University of Illinois, which are partially supported by the U.S. Department of Energy under grants DE-FG02-07ER46453 and DE-FG02-07ER46471. We also acknowledge the support by the National Science Foundation (CHE 04-02420). S.K.G. was supported by the Office of Basic Energy Sciences, Division of Chemical Sciences, Geosciences, and Biosciences, U.S. Department of Energy (DE-AC02-06CH11357). We also thank the transmission and scanning electron microscope teams, especially Dr. Jianguo Wen, at the Frederick Seitz Materials Research Laboratory and the Imaging Technology Group at the Beckman Institute for Advanced Science and Technology.

Supporting information for this article is available on the WWW under <http://www.angewandte.org> or from the author.

cylindrical depressions were about 456, 350, and 748 nm, respectively. A continuous Au layer was formed on the embossed polymer by sputter deposition in 5 mTorr of Ar (Figure 1a). The high-resolution SEM insets of Figure 1a

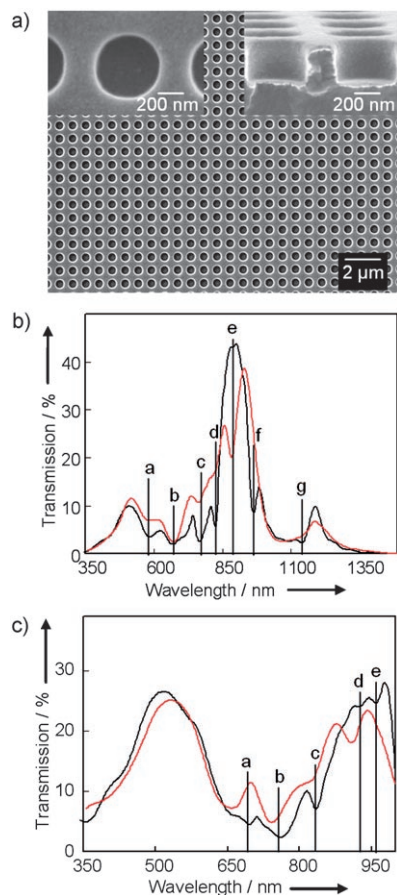


Figure 1. Images and transmission spectra of a 3D plasmonic crystal. a) Scanning electron micrographs (SEM) of a crystal. Left inset: A top-view SEM that shows the approximate nanowell diameter. Right inset: A high-magnification SEM that shows the continuous Au layer on the surface of the nanowell array. b) Normal-incidence transmission spectrum of a plasmonic crystal in air (red) and rigorous electrostatics modeling of the spectrum (black). The features labeled a, b, and c correspond to BW-SPPs, feature d arises from a combination of an LSPR and a WA, and features e, f, and g correspond to LSPRs. c) Normal-incidence transmission spectrum of a crystal in water (red) and rigorous electrostatics modeling of the spectrum (black). The features labeled a and b correspond to BW-SPPs, features c and d correspond to LSPRs, and feature e arises from a combination of an LSPR and a WA.

clearly show the formation of a continuous Au layer on the embossed polymer nanowells. Transmission electron microscopy (TEM) was used to measure the thickness of the Au layer on the top surface of the crystal and on the sidewall and bottom of the nanowells (ca. 35, 12, and 20 nm, respectively; Supporting Information, Figure S2). This gold coverage is different from that of our previously reported quasi-3D plasmonic crystals, in which the top layer of gold was physically separate from the gold at the bottom of the nanowells.

Full 3D FDTD calculations with appropriate periodic boundary conditions were used to model the normal-incidence transmission spectrum of a 3D crystal in air (Figure 1b).^[17,18] Good agreement between experiment and theory required careful consideration of the Au film thickness on the nanowell array as measured by TEM (Supporting Information, Figure S3). Fourier transforms of the FDTD results revealed that the strong peak near 900 nm is primarily due to a localized surface plasmon resonance (LSPR) of the nanowells with large near-field intensities close to the walls and spanning across the opening of the nanowells (Supporting Information, Figure S4). Other features in the spectra can be assigned to LSPRs, Bloch wave SPPs (BW-SPPs), and Wood's anomalies (WAs), or a combination of these, and the background thin-film transmission of Au at about 500 nm (Figure 1b).^[13,17] For example, an approximate relation for the allowed wavelengths λ of BW-SPPs excited by normal-incidence illumination on a square array of subwavelength holes in a metal film predicts lowest order BW-SPPs associated with the air/metal interfaces near 564 and 764 nm, which correlate well with the spectral features observed near these λ values in Figure 1b.

Full 3D FDTD calculations were also used to model the normal-incidence transmission spectrum of a 3D crystal in contact with water (i.e., the air/metal interface was replaced with a water/metal interface, as is encountered in real-time biosensing in solution). Figure 1c shows the experimental and theoretical transmission spectra of a 3D crystal in contact with water in the range of 350–1000 nm. Note that the plasmonic features associated with the water/metal interface are, in general, red-shifted relative to those for the air/metal interface, as is expected for an increase in the surrounding dielectric constant. The FDTD calculations did not include water absorption, which becomes important for $\lambda > 1000$ nm and probably accounts for the theoretical/experimental differences in the higher λ range of Figure 1c.

As shown in Figure 1b and c, the sensitivity of a 3D plasmonic crystal arises as a consequence of the significant intensity of, principally, BW-SPPs and LSPRs spanning the region of about 600–850 nm. Through 3D FDTD calculations, we found that the sensitivity of these modes (for modest variations around the current design rules) increases as the diameter of the hole increases, the center-to-center spacing of the holes decreases, the nanowell depth increases, and as the thickness of the gold on the top surface, sidewalls, and bottoms of the nanowells decreases.

The multispectral sensitivity of the 3D plasmonic crystal to changes in bulk refractive index is shown in Figure 2. Spectra were collected as a function of time as solutions of increasing concentration (0–5.6 wt %) of poly(ethylene glycol) (PEG, $M = 10000$) were passed through a fluid-flow cell containing a 3D crystal (Supporting Information Figure S5). The series of spectra were then referenced to the spectrum at time $t = 0$ to generate the difference map in Figure 2a, which shows the changes in transmission (due to changes in peak position and intensity) over a broad range of wavelengths as the refractive index of the solution in the flow cell was increased.

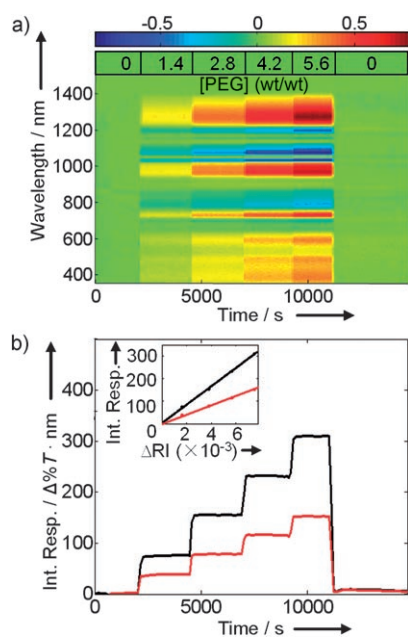


Figure 2. Multispectral plasmonic response of a 3D plasmonic crystal to injections of increasing concentrations of aqueous PEG solutions. a) Contour plot of the change in transmission (%T) as a function of wavelength and time (with the corresponding injected PEG concentrations indicated on the plot). b) Integrated response (Int. Resp.) of a plasmonic crystal as a function of time over the wavelength ranges of 355–1500 nm (black) and 355–1000 nm (red). Inset: The corresponding linear correlation between Int. Resp. and the change in refractive index of the PEG solutions for the two analyzed wavelength ranges.

The sensitivity of a plasmonic sensor to bulk refractive index is often determined by measuring the position of a single resonance or the intensity (e.g., extinction) at a single wavelength as a function of the refractive index of the surrounding fluid. Several 3D crystals were tested, and in terms of this figure of merit (FOM), the most responsive features exhibited linear peak position shifts and magnitude changes with sensitivities of about $700\text{--}800\text{ nm RIU}^{-1}$ at 1024 nm and $\approx 3.5\text{ Abs RIU}^{-1}$ at 1077 nm (RIU defined as refractive index unit), respectively (Supporting Information, Figure S6). These values exceed the bulk refractive index sensitivities reported for most 2D nanohole (ca. 400 nm RIU^{-1}) and nanoparticle arrays ($76\text{--}200\text{ nm RIU}^{-1}$, 0.46 Abs RIU^{-1}).^[19–26]

A more appropriate FOM for an imaging sensor, in analogy with the functioning of the eye, is one that accounts for both wavelength- and intensity-based contributions to its optical response. To this end, we integrated the total spectral response of the PEG calibration, measured as the absolute value of difference spectra, over accessible wavelengths (355–1500 nm) as a function of time.^[13] This protocol yields the single response curve shown in Figure 2b (black). The integrated response of the 3D plasmonic crystal changed linearly with the refractive index of the PEG solution (Figure 2b, inset, black) with a sensitivity of about $40000\text{ } \Delta\%T\text{ nm RIU}^{-1}$, which is 1.6 times greater than the integrated bulk refractive index sensitivity of the quasi-3D plasmonic crystals reported in our earlier work (ca.

$25000\text{ } \Delta\%T\text{ nm RIU}^{-1}$).^[13] Most of the enhancement in sensitivity originates from significant increases in the plasmonic response at visible wavelengths (Figure 2b, red). This is evident by comparing the integrated sensitivities of the 3D (Figure 2b, inset, red) and quasi-3D plasmonic crystals in the wavelength range of 355–1000 nm, which are about 20000 and $6000\text{ } \Delta\%T\text{ nm RIU}^{-1}$, respectively.

The spectral features of a full 3D plasmonic crystal in air or water are blue-shifted relative to the spectral features of a quasi-3D plasmonic crystal (Supporting Information, Figure S7), which accounts for this greater visible wavelength sensitivity. As the array geometry (diameter, spacing, and depth of the nanoholes) of the full 3D plasmonic crystals is similar to that of the previously reported quasi-3D plasmonic crystals, the difference in spectral sensitivity must arise principally from effects due to the geometry of the metal. Changing the metal thickness on a full 3D plasmonic crystal strongly affects the width and magnitude of the peaks, but only weakly shifts the position of the spectral features (Supporting Information, Figure S8). The blue shift of the spectral features—and greater visible-wavelength sensitivity—of the full 3D plasmonic crystals can therefore be attributed to the architectural differences of the gold (the full 3D crystal has a conformal metal film on the embossed polymer, whereas the quasi-3D crystal consists of a gold nanohole array that is physically separated from the gold disks at the bottoms of the nanowells).

The increase in sensitivity at visible wavelengths, together with the high levels of spatial uniformity of the crystals, has important implications for monitoring/seeing binding events over large areas with a common laboratory optical microscope. Figure 3 demonstrates this by showing transmission-mode images of a well-defined model system—a 1-octadecanethiol (ODT) self-assembled monolayer (SAM)^[27]—patterned on the surface of a 3D plasmonic crystal by micro-contact printing (μCP).^[28] The printed ODT regions (boxes and rectangles) show greater transmission than the surrounding unmodified areas of the plasmonic crystal (Figure 3a). The single pixel line profile shown in Figure 3b illustrates the high signal-to-noise ratio obtained when imaging SAMs about 2 nm in thickness.^[29] Analysis of the step edge at the ODT-patterned and unmodified regions of the 3D crystal was performed by convolving a step function and a Gaussian (Figure 3b, inset) to assess the spatial resolution of the 3D-integrated sensor; these data are well fit by a Gaussian width of $\sigma = 3\text{ }\mu\text{m}$, a value that is slightly larger than the resolution limit of the camera and imaging optics ($1.6\text{ }\mu\text{m}$). In further support of this point, patterns of μCP lines of ODT as small as about $8\text{ }\mu\text{m}$ wide spaced by about $15\text{ }\mu\text{m}$ have also been imaged with full spatial resolution (Supporting Information, Figure S9). The most significant feature of the images presented here, which were obtained with white-light illumination, is that their contrast is due to an integrated response of the camera to spectroscopic changes occurring predominantly in the visible region of the spectrum (no wavelength-selecting filters were used).

The submonolayer sensitivity of a 3D plasmonic crystal is highlighted by the data presented in Figure 4. A patterned SAM of ODT was formed on a plasmonic crystal by μCP

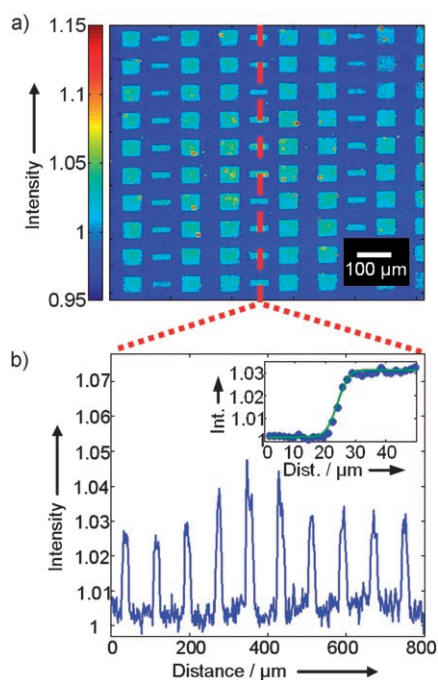


Figure 3. Transmitted-light images of μ CP ODT monolayers on a plasmonic crystal. a) An array of squares and rectangles of ODT imaged with a $10\times$ objective. b) Vertical line profile through the image in panel (a). Inset: A measured step edge (blue symbols) and a fitted step edge (green curve) with a Gaussian width of about $3\ \mu\text{m}$.

(Figure 4a, red features), followed by controlled formation of a second SAM of 1-hexadecanethiol (HDT) in the originally unmodified areas of the crystal by immersing the ODT-patterned crystal into an ethanolic solution of HDT (“backfilling”). Transmitted-light optical images of the sample were collected before and after backfilling at specific time intervals to measure the effect of HDT backfilling on the image contrast (defined here as the image intensity of the ODT-patterned areas minus the image intensity of the surrounding areas of the crystal). Before backfilling, the μ CP ODT patterns were clearly visible with an image contrast of about 0.05 ± 0.01 (Figure 4a) due to the refractive-index difference between the ODT-patterned and unpatterned areas. Backfilling with HDT decreased the image contrast (Figure 4b), since HDT adsorption onto the 3D crystal reduced the refractive-index difference between the ODT regions and the surrounding areas at the surface of the crystal. The ODT pattern is still visible, although less distinct, after backfilling with HDT for 5 min (Figure 4b). Figure 4c shows a decrease in plasmonic image contrast as a function of backfilling time that resembles an inverted first-order Langmuir adsorption isotherm. This plot illustrates the exquisite analytical sensitivity of these 3D plasmonic crystals, which can be used to differentiate between adsorbates with a mass difference of about 25 amu. Independent analyses based on SEM images (an imaging technique that also has submonolayer sensitivity; Supporting Information, Figure S10) confirm formation of this patterned SAM.^[30]

The loss of image integrity in Figure 4b can be attributed to several factors including: 1) the ODT SAM formed by μ CP

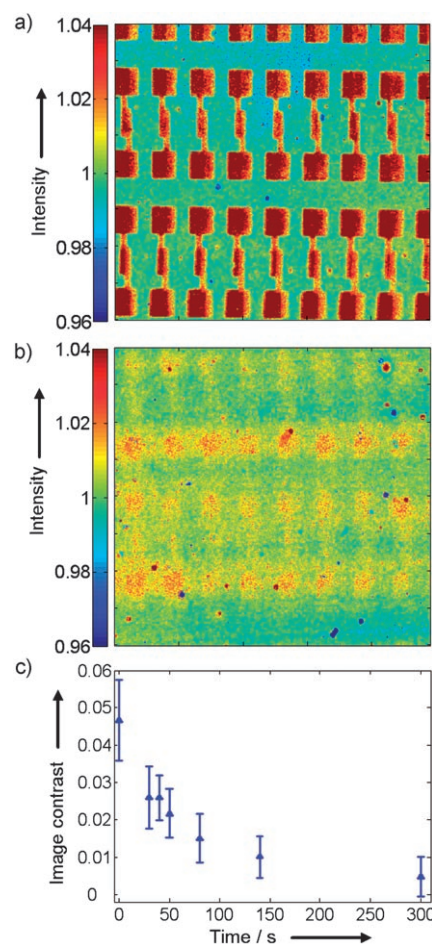


Figure 4. Optical detection of submonolayer quantities of alkanethiols. a) Transmitted-light image of a μ CP ODT pattern (red features, the red boxes at the ends of each feature have dimensions on the order of 50 microns) on a 3D plasmonic crystal. b) Transmitted-light image of the sample after a 300 s of backfilling with HDT; same scale as (a). c) Plot of image contrast (ODT intensity minus HDT intensity) as a function of the HDT backfilling time.

on the rough, polycrystalline Au substrate sputtered on the nanostructured plastic surface contains many defect sites that can be filled by HDT;^[27] and 2) SAMs are dynamic systems in which site exchange can occur between the ODT and HDT molecules during the backfilling procedure (control data suggest that as much as 30% of the ODT SAM can exchange during backfilling).^[27,31] These factors complicate plasmonic imaging, since mixing of HDT and ODT on the surface of the crystal will diminish the differences in the refractive-index gradients sensed in the ODT and HDT regions of the crystal. Even so, the self-normalized (i.e., relative) magnitude of the gray-scale contrast seen between the HDT and ODT regions is instructive (we use the normalized value to account for any drift in the intensity of the illumination source). Backfilling reduces the relative contrast to about 10% of its initial value. This correlates remarkably well with the fact that the 25-amu difference between HDT and ODT corresponds to about 11% difference in their chain length, the structural feature that would serve to directly scale the refractive index supported by each SAM. This strongly suggests an ideal, and

essentially linear, white-light response of a CCD camera using this plasmonic sensor.

We have developed a new type of 3D plasmonic crystal that is more sensitive than a previously reported quasi-3D plasmonic sensor^[13] by simply changing the geometry of the gold deposited on the nanostructured surface of the crystal. These inexpensive, easily fabricated 3D plasmonic crystals can be used to image surface adsorbates with exceptional analytical sensitivity and spatial resolution at visible wavelengths. These features, together with the high spatial uniformity of the crystals, make them promising platforms for the development of microarrays that allow label-free detection of analytes by eye.

Experimental Section

For materials and experimental details, see Supporting Information.

Received: January 31, 2008

Published online: May 30, 2008

Keywords: analytical methods · optical imaging · sensors · surface plasmon resonance

-
- [1] W. Knoll, *Annu. Rev. Phys. Chem.* **1998**, *49*, 569–638.
- [2] M. E. Stewart, C. R. Anderton, L. B. Thompson, J. Maria, S. K. Gray, J. A. Rogers, R. G. Nuzzo, *Chem. Rev.* **2008**, *108*, 494–521.
- [3] J. Homola, *Anal. Bioanal. Chem.* **2003**, *377*, 528–539.
- [4] N. Zhang, R. Schweiss, Y. Zong, W. Knoll, *Electrochim. Acta* **2007**, *52*, 2869–2875.
- [5] O. Telezhnikova, J. Homola, *Opt. Lett.* **2006**, *31*, 3339–3341.
- [6] H. J. Lee, D. Nedelkov, R. M. Corn, *Anal. Chem.* **2006**, *78*, 6504–6510.
- [7] J. S. Shumaker-Parry, R. Aebbersold, C. T. Campbell, *Anal. Chem.* **2004**, *76*, 2071–2082.
- [8] Y. Li, H. J. Lee, R. M. Corn, *Anal. Chem.* **2007**, *79*, 1082–1088.
- [9] B. K. Singh, A. C. Hillier, *Anal. Chem.* **2007**, *79*, 5124–5132.
- [10] K. A. Tetz, L. Pang, Y. Fainman, *Opt. Lett.* **2006**, *31*, 1528–1530.
- [11] V. Malyarchuk, F. Hua, N. H. Mack, V. T. Velasquez, J. O. White, R. G. Nuzzo, J. A. Rogers, *Opt. Express* **2005**, *13*, 5669–5675.
- [12] V. Malyarchuk, M. E. Stewart, R. G. Nuzzo, J. A. Rogers, *Appl. Phys. Lett.* **2007**, *90*, 203113.
- [13] M. E. Stewart, N. H. Mack, V. Malyarchuk, J. A. N. T. Soares, T.-W. Lee, S. K. Gray, R. G. Nuzzo, J. A. Rogers, *Proc. Natl. Acad. Sci. USA* **2006**, *103*, 17143–17148.
- [14] T. W. Ebbesen, H. J. Lezec, H. F. Ghaemi, T. Thio, P. A. Wolff, *Nature* **1998**, *391*, 667–669.
- [15] W. L. Barnes, W. A. Murray, J. Dintinger, E. Devaux, T. W. Ebbesen, *Phys. Rev. Lett.* **2004**, *92*, 107401.
- [16] R. Gordon, A. G. Brolo, A. McKinnon, A. Rajora, B. Leathem, K. L. Kavanagh, *Phys. Rev. Lett.* **2004**, *92*, 037401.
- [17] S.-H. Chang, S. K. Gray, G. C. Schatz, *Opt. Express* **2005**, *13*, 3150–3165.
- [18] A. Taflove, S. C. Hagness, *Computational Electrodynamics: The Finite-Difference Time-Domain Method*, 3rd ed., Artech House, Boston, **2005**.
- [19] A. G. Brolo, R. Gordon, B. Leathem, K. L. Kavanagh, *Langmuir* **2004**, *20*, 4813–4815.
- [20] A. Dahlin, M. Zach, T. Rindzevicius, M. Kall, D. S. Sutherland, F. Hook, *J. Am. Chem. Soc.* **2005**, *127*, 5043–5048.
- [21] A. B. Dahlin, J. O. Tegenfeldt, F. Hook, *Anal. Chem.* **2006**, *78*, 4416–4423.
- [22] E. M. Hicks, X. Zhang, S. Zou, O. Lyandres, K. G. Spears, G. C. Schatz, R. P. Van Duyne, *J. Phys. Chem. B* **2005**, *109*, 22351–22358.
- [23] A. D. McFarland, R. P. Van Duyne, *Nano Lett.* **2003**, *3*, 1057–1062.
- [24] N. Nath, A. Chilkoti, *Anal. Chem.* **2002**, *74*, 504–509.
- [25] T. Rindzevicius, Y. Alaverdyan, A. Dahlin, F. Hook, D. S. Sutherland, M. Kall, *Nano Lett.* **2005**, *5*, 2335–2339.
- [26] D. A. Stuart, A. J. Haes, C. R. Yonzon, E. M. Hicks, R. P. Van Duyne, *IEE Proc. Nanobiotechnol.* **2005**, *152*, 13–22.
- [27] J. C. Love, L. A. Estroff, J. K. Kriebel, R. G. Nuzzo, G. M. Whitesides, *Chem. Rev.* **2005**, *105*, 1103–1169.
- [28] A. Kumar, H. A. Biebuyck, G. M. Whitesides, *Langmuir* **1994**, *10*, 1498–1511.
- [29] C. D. Bain, E. B. Troughton, Y. T. Tao, J. Evall, G. M. Whitesides, R. G. Nuzzo, *J. Am. Chem. Soc.* **1989**, *111*, 321–335.
- [30] N. H. Mack, R. Dong, R. G. Nuzzo, *J. Am. Chem. Soc.* **2006**, *128*, 7871–7881.
- [31] H. A. Biebuyck, C. D. Bain, G. M. Whitesides, *Langmuir* **1994**, *10*, 1825–1831.
-